

This is a peer-reviewed, accepted author manuscript of the following research article: Zong, C., Zheng, F., Chen, D., Dempster, W., & Song, X. (2020). Computational fluid dynamics analysis of the flow force exerted on the disk of a direct-operated pressure safety valve in energy system. *Journal of Pressure Vessel Technology, Transactions of the ASME*, 142(1), [011702].

<https://doi.org/10.1115/1.4045131>

Computational Fluid Dynamics Analysis of the Flow Force Exerted on the Disk of a Direct Operated Pressure Safety Valve in an Energy System

Chaoyong Zong, Fengjie Zheng, Dianjing, Dempster William, Song Xueguan*

Department of Mechanical and Aerospace Engineering, University of Strathclyde, Glasgow G1 1XJ, UK

National Engineering Research Center for Special Pump and Valve, Beijing 9200-11, China

School of Mechanical Engineering, Dalian University of Technology, Dalian 116023, China

Abstract

The flow force acting on a valve disk plays an important role in the overall performance of pressure safety valves (PSVs). To quantify the disk force, computational fluid dynamics (CFD) methods have been widely implemented. In this paper, the capability of CFD models, and the identification of the most suitable turbulence models' geometry modeling and mesh requirements have been assessed to establish the accuracy of CFD models for disk force prediction. For validation purposes, a PSV disk force measuring rig was designed and constructed to obtain the steady-state flow forces exerted on the valve disk at different valve openings. The CFD model assessment is achieved by comparing the simulation results to experimental measurements; this is achieved in two stages. Stage 1 investigates the use of Reynolds averaged Navier–Stokes (RANS)-based turbulence models where two-dimensional (2D) simulations are performed with five turbulence models. The results indicate that a variety of force results are produced by different turbulence models, among which the shear stress transport (SST) $k-x$ was found to have the best performance. Stage 2 investigates meshing and the use of symmetry and geometry simplifications; 2D, 1/8 three-dimensional (3D) and 1/2 3D mesh models are examined. The results indicate that the 1/8 3D mesh model is the optimal choice, owing to its higher accuracy and reasonable grid scale. The studies performed in this paper extend the knowledge of compressible flow force prediction, and should facilitate the design or optimization of PSVs.

[DOI: 10.1115/1.4045131]

1 Introduction

Valves are widely applied in pressure/energy systems to control the pressure, flow, and/or the direction of the flow [1,2]. One such valve, the direct-operating pressure safety valves (PSVs) are widely used in various pressure-related systems, to ensure that the system pressure remains within a designated range [3]. Under specific conditions, direct-operated PSVs may demonstrate dynamic unstable behaviors, such as chattering, fluttering, or low frequency cycling [1,4–6], which may severely damage the valve structure or impair the overall performance and possibly compromise overall plant safety. Previous research indicates that fluid–structure interaction, i.e., the interaction between the flow force and the disk motion, is a potential cause of these dynamic instabilities [7,8]. The fluid force is complex and difficult to quantify theoretically, owing to the nonlinear nature of the flow due to the existence of shocks and the highly compressible turbulent nature of the flow conditions.

There are three commonly used methods for fluid disk force investigations; experimental methods, analytical methods, and computational fluid dynamics (CFD) methods. Experimental methods produce the most convincing results, but the local flow details are largely unknown. Furthermore, experimental methods are relatively straightforward but limited to the test conditions of the facility and generally do not cover the full operating

conditions of the valve. Analytical methods have the advantages of being much more efficient and cost-effective but are limited by the simplifying assumptions required and not suitable for accurately quantifying the flow force when the flow path is irregular [9]. CFD methods have the advantages of high efficiency, provide detailed analysis of the flow behavior economically, and have been widely used in flow force-related investigations.

Computational fluid dynamics models such as turbulence models and mesh models have a significant influence on the fluid generated disk force prediction [9,10]. For example, Lisowski et al. [11] conducted an experimental and numerical study on a conventional hydraulic control valve with the purpose of reducing the flow force acting on the valve spool. A three-dimensional (3D) mesh model incorporating a $k - e$ turbulence model was developed and adopted for flow force simulations. The predicted flow forces are compared with measured forces at seven valve openings. The turbulence model either underestimated or overestimated the measured flow forces, with the deviation increasing with the mass flow rate. The maximum deviation was 10%. Similarly, Simic and Herakovic [12] conducted a series of CFD and experimental investigations on a seat valve to investigate the flow force exerted on the valve spool. Comparisons were made between the experiments and CFD simulations. The results indicated that the shear stress transport (SST) $k - w$ turbulence model is more accurate than the $k - e$ and $k - w$ turbulence models in flow force predictions. The flow forces were overestimated at almost all valve openings when the $k - e$ and $k - w$ turbulence models were used.

Amirante et al. [13] conducted a CFD analysis on a hydraulic proportional valve for the purpose of discovering the influence of critical valve parameters on the flow force acting on a valve spool. The mass flow rate obtained from simulations and experiments were compared and used to validate the CFD models. The results indicated that the renormalization group (RNG) $k - e$ turbulence model is suitable for further investigations. Scuro et al. [14] conducted a CFD investigation on the steady-state flows of a directly operated safety relief valve, which indicated that the fluid forces are overestimated when using a theoretical approach. The CFD model was validated by comparing the simulated flow contour with that obtained from experiments instead of comparing the flow force directly. However, whether this validated CFD model is also suitable for flow force predicting is uncertain and is not discussed. Asim et al. [15] performed a series of CFD analyses on a multistage severe service control valve, aiming to identify the effect of alternative trim geometries and other settings on the flow coefficient. A 3D unstructured mesh model was built, and the SST $k - w$ model was adopted for mass flow rate prediction. Predicted flow rates were compared with measured flow rates at four valve openings. The results indicated that the average deviation between simulations and experiments is 1.60%, confirming the ability of the SST $k - w$ turbulence model to accurately predict the flow rate. However, the ability of the SST $k - w$ turbulence model to predict the flow force is not mentioned. Dempster et al. [16] carried out experimental and CFD studies on a refrigeration type safety valve and showed that, using a two-dimensional (2D) axisymmetric model with a structured grid mesh, both the forces and flows could be well predicted using $k - e$ turbulence models. Deviations were believed to be associated with dimensional inaccuracies of small features such as filets, and edge rounding. Dempster and Alshaikh [17] extended these studies by examining the forces in the same valve types for two-phase air–water flows. Comparisons were made between the simulations and experiments, and the results showed good agreement.

The above-mentioned research studies indicate that the combination of experimental and CFD methods have been widely used for flow force related investigations. However, there are still some issues that need to be clarified. The first one is regarding the turbulence model, i.e., which turbulence model is optimal for predicting flow force is uncertain. The second issue considers possible geometrical simplifications. For flows having axisymmetric geometry structures, some researchers adopt a 2D mesh model for flow force prediction, while other researchers still adopt a 3D mesh model. The extent of differences between 2D and 3D mesh models on flow force prediction is uncertain. To the authors' knowledge, few studies in the open literature have quantified this issue. Finally, the majority of studies are focused on valves or components where incompressible flow conditions dominate; few studies have been published investigating the force under the more demanding compressible flow.

In the present study, numerical and experimental investigations have been carried out on a modified spring-loaded PSV with air as the working fluid to investigate the abilities of CFD models and the accuracy of different turbulence models and mesh configurations for flow force predictions. Comparisons are made at various valve openings under steady-state conditions. The main objective is to identify the optimal CFD model with which the flow force in compressible flows can be quantified accurately. This is believed to be a prerequisite for any future investigations involving CFD based dynamic instability investigation of PSVs. Finally, since the availability of experimental data is scarce, the data obtained during this study are provided along with the associated controlling geometry so that other researchers can examine the use of CFD for this complex flow condition (see Appendix A).

The key points pursued in the paper can be summarized as follows: (i) the measurement of the disk flow force at different valve openings; (ii) the performance of CFD simulations with different turbulence models and mesh configurations; (iii) the comparison of the simulation and experimental results to identify the optimal CFD model. These aspects are discussed in full in the paper.

2 Details of Direct-Operated Pressure Safety Valves

A conventional direct-operated PSV is a self-actuated spring loaded valve, which is designed to protect pressurized systems from over-pressure [18]. There are three critical components in the direct-operated PSV, the nozzle, the valve disk and the spring. All of them have significant influence on the overall performance of the valve. Figure 1 shows a schematic diagram of a direct-operated PSV. The nozzle is inserted into the valve body and connected to the piping/vessel by thread or flange connections. When closed, the valve disk is seated on the nozzle and compressed by a spring. When the system pressure exceeds the valve set pressure, the disk will lift, fluid will discharge and the system pressure will drop. For different lift positions, the geometries of the flow path are different, which changes the pressure distribution on the valve disk and hence the force. The valve design and corresponding performance is directly related to the disk force behavior.

3 Valve Test Rig

To test the abilities of CFD models, an experimental test rig was designed and built to measure the steady-state flow force at different valve openings. Figure 2(a) shows the schematic diagram of the test rig. The vessel has a capacity of 0.3m^3 and is used as the compressed air supply. The solenoid valve has an inner diameter of 40mm and is powered by a 24V DC supply. The inner diameter of the pipe is 0.026m, which is equal to that of the PSV inlet. A total of five pressure sensors are installed in the test rig with the purpose of measuring the static pressure at different positions. The range of these sensors is 0–6 bars, with a measurement accuracy of 0.5% of range. With the purpose of recording and processing the sensor signals, a data processing system was developed with a National Instruments data acquisition unit and LabVIEW 2018 software platform. The sampling frequency was 5000Hz. Figure 2(b) shows a schematic diagram of the tested PSV (see the specific parameters in Appendix B). For the purpose of facilitating installation and visualization, the valve body was not included, and the air was free to discharge into the atmosphere. Under this condition, the back pressure normally found in a PSV is not present resulting in the disk forces (in the test valve) being dominated by the pressure distributions on the front face of disk. This region is where the most challenging compressible fluid flows exist. Because the primary purpose is to assess the ability of CFD models, it was decided to isolate the effects of the front face from the valve body to allow a clearer and direct assessment of the models. However, this was at some expense to what might occur in an actual valve. In addition, the lower adjusting ring, normally used in safety valves to control opening conditions, was modified to better match axis-symmetric geometry conditions. Standard adjusting rings normally include notches regularly

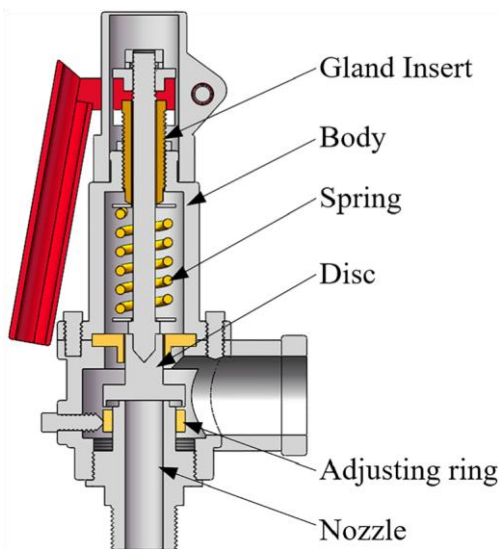


Fig. 1 Schematic of the direct-operated PSV

arranged in the ring body to allow locking of the ring movement. In the ring used in this study, the notches have been neglected, resulting in a smooth surface free from any 3D effects.

In order to control the disk position independently, a mechanical mechanism was installed in the modified PSV, with an adjustment accuracy of 0.01mm. The flow force acting on the disk was measured by a load cell inserted into the valve spindle. The load cell had a range of 0–100N with a measurement accuracy of 0.03% of its range. However, it was observed that when under load, the load cell deforms slightly, leading to changes in the valve disk position and resulting in an increase of the measured flow force. In order to obtain accurate data of the valve disk position, a laser displacement sensor was installed on the PSV and a rigid strip was fixed to the valve spindle to facilitate accurate disk position measurement. The range of the laser displacement sensor was 25–35mm and the measurement accuracy was 0.001mm. In order to monitor the mass flow rate in real-time, an Emerson F100S series Coriolis mass flowmeter was installed in the piping system. The range of the flowmeter was 0.05–0.20kg/s, with a measurement accuracy of 0.50% of the flow rate. The whole system was pressurized by an air compressor with a capacity of 100L/min (not shown in Fig. 2).

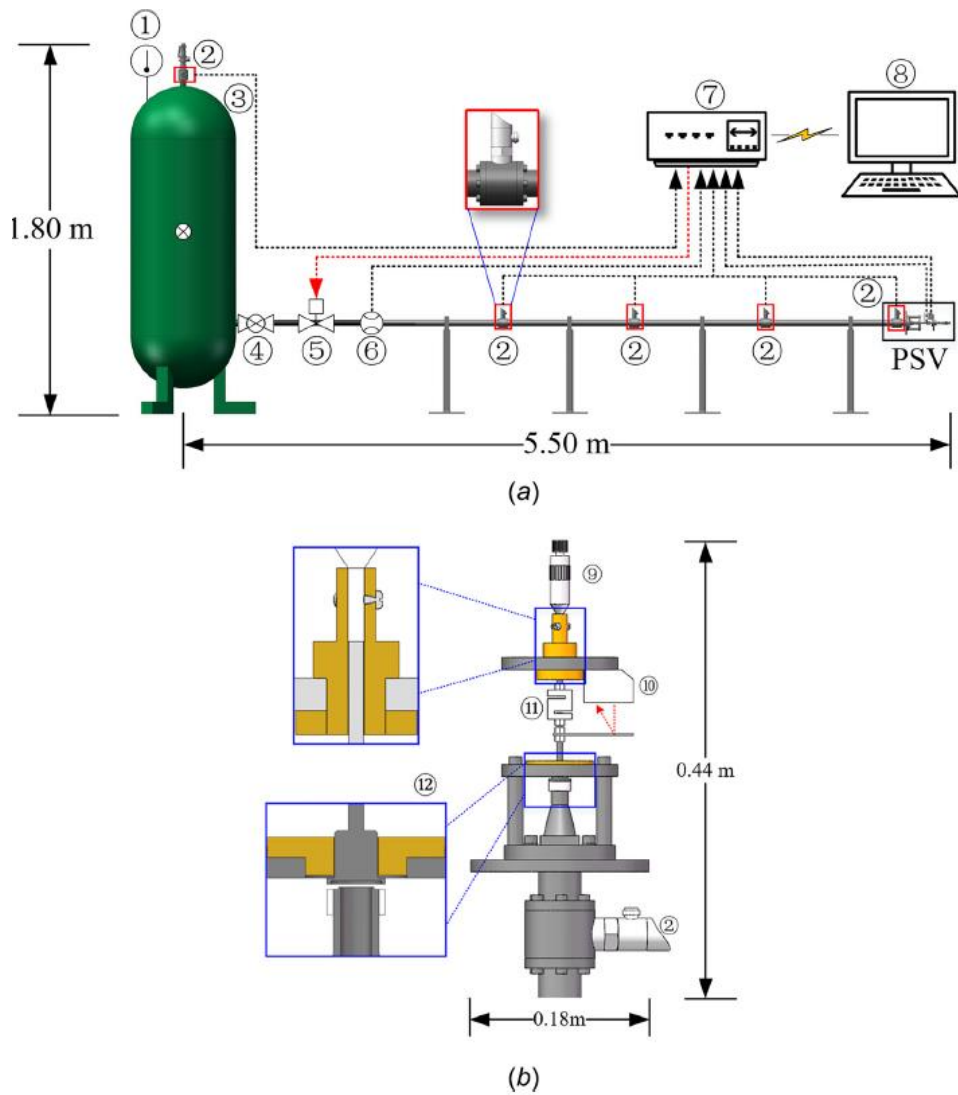


Fig. 2 Schematics of flow force measuring rig: (a) schematic diagram of test rig and (b) schematic diagram of modified PSV. ←—Thermometer, →—pressure sensor, fi—vessel, fl—ball valve, ——solenoid valve, ——mass flow sensor, †—DAQ (data acquisition), ‡—personal computer, ——feeding mechanism, ——displacement sensor, (11)—load cell, and (12)—nozzle, disk and adjustment ring.

Since the air supply vessel was finite, it could not sustain a steady pressure for the valve discharge flows. The tests were therefore conducted under slowly varying transients to determine that data. For example, taking a 3.00bar static inlet pressure as a typical test condition, the methodology followed consisted of the following steps for any approximately set disk displacement: (i) closing the solenoid valve and pressurizing the vessel to a pressure higher than 3.00bar, such as 3.50 or 4.00bar, and (ii) opening the solenoid valve to reduce the vessel

pressure to a value lower than 3.00bar, such as 2.50bar. Over the whole process, the data acquisition system recorded the inlet pressure, disk force, mass flow rate, and valve opening in real-time. It was observed that the inlet pressure, disk force, and mass flow rate decreased steadily and nearly linearly when the fluid was being discharged. Establishing the time when the inlet pressure was equal to 3.00bar enabled the corresponding lift force (and exact disk lift position) to be determined for the specific valve opening conditions.

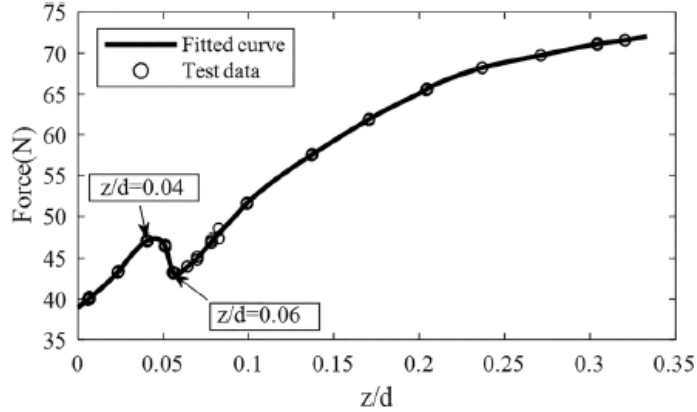


Fig. 3 Experimental flow force

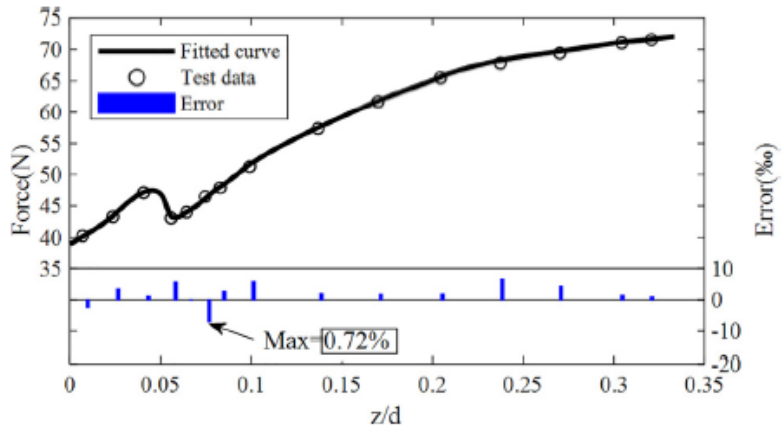


Fig. 4 Validation of the GPR fitting

Figure 3 illustrates the results obtained from the tests, where a 3bar inlet pressure condition was maintained (as indicated in Appendix A). Symbols denote the flow forces at different openings and overlaps indicate at least two measurements for each valve opening. For the disk lift, a dimensionless index z/d is introduced, where z is the lift of the valve disk and d is the inner diameter of the nozzle. It can be seen that good reproducibility is achieved.

The primary purpose of performing the experimental test is to validate CFD models by comparing CFD predicted force-lift characteristics to those measured. For simulation, the valve opening is easy to define using the capabilities available through computer aided design (CAD) modeling. On the contrary, during the test, the exact disk position was difficult to maintain at a desired value, owing to the aforementioned deformation of the load cell. To overcome this, a Gaussian process regression (GPR) method was adopted to fit a continuous curve to the flow force-lift data, as shown in Fig. 3.

To validate the accuracy of the fitted curve, an additional test was carried out, and an error index was defined to assess the deviations between the experimental data and the fitted curve. The error was defined as error

$$\text{error} = (F_{\text{Predicted}} - F)/F_{\text{Predicted}} \times 100\% \quad (1)$$

where $F_{\text{Predicted}}$ is the force obtained by GPR fitting, and F denotes the force obtained by the additional experiment.

Figure 4 shows the result of the validation, where the bars represent the errors at different openings. It can be seen from the figure that for all valve openings, the maximum error is 0.72%, which was deemed acceptable. Therefore, the fitted curve was set to be a criterion for the forthcoming validations of CFD models. The experimental measured force data for various disk lifts and the dimensions of the key geometry features of the nozzle, valve seat, and disk are provided in Appendices A and B.

4 Numerical Analysis

A series of simulations to reproduce the test conditions were performed with the commercial code ANSYS FLUENT 18.0. The details of the CFD simulations, including basic theory, fluid domain modelling, mesh grid generations, and solver settings, are discussed as follows.

4.1 Basic Theories. The principle of CFD simulation is to solve the governing equations with given boundary conditions in designated fluid domains [12]. The governing equations are the conservation equations regarding mass, momentum, and energy as well as other additional equations. In FLUENT, conservation equations of mass and momentum are essential for all flow cases [19], and they can be written as follows: Mass conservation equation

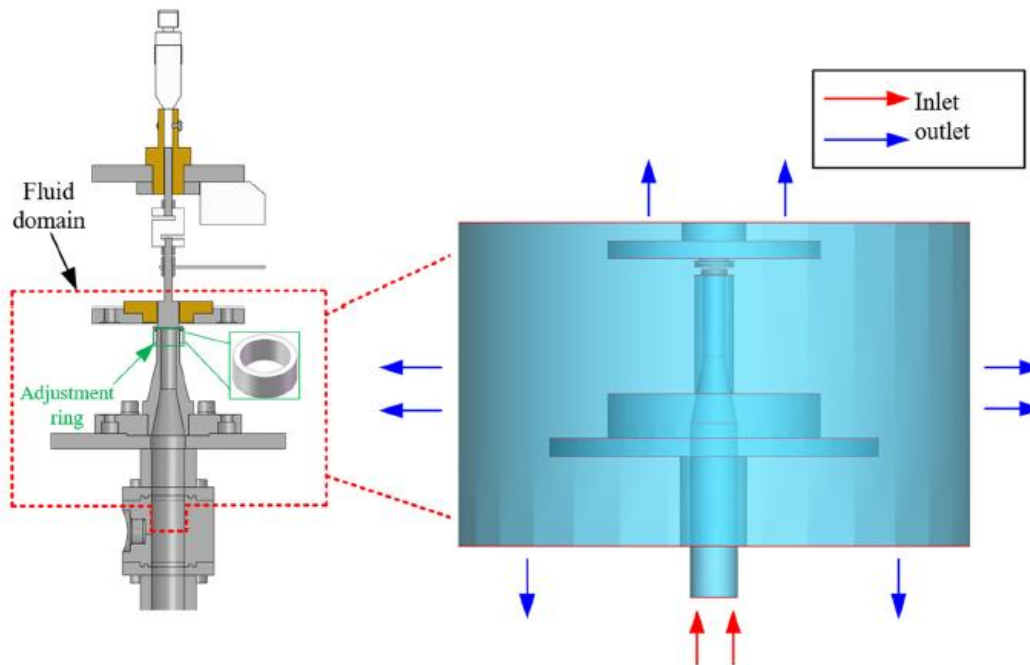


Fig. 5 Schematic of the fluid domain

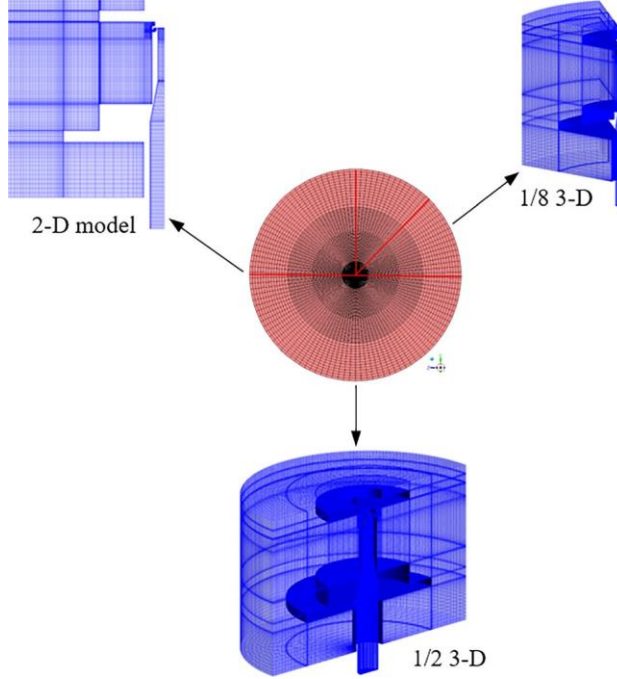


Fig. 6 Different mesh models for PSV

mass conservation equation:

$$\frac{\partial \rho}{\partial t} + \nabla \cdot (\rho v^r) = S_m \quad (2)$$

momentum conservation Equation:

$$\frac{\partial}{\partial t}(\rho v^r) + \nabla \cdot (\rho v^r v^r) = -\nabla p + \nabla \cdot (\bar{\tau}) + \rho g^r + F \quad (3)$$

$$\text{and } \bar{\tau} = \mu \left[(\nabla v^r + \nabla v^{rT}) - \frac{2}{3} \nabla \cdot v^r I \right] \quad (4)$$

where ρ denotes density, v denotes velocity, S_m denotes items of source, p denotes static pressure, s denotes stress tensor, qg denotes gravitational body force, F denotes external body forces, I denotes molecular viscosity, and I denotes the unit tensor.

Due to the nonlinearity and multiscale features of turbulence, directly solving these governing equations is extremely difficult. To overcome this, an alternative approach using the Reynolds averaged Navier–Stokes (RANS) method is available whereby the instantaneous quantities are divided into time-averaged and fluctuating quantities [19]. However, the closure of the RANS equations requires models for the Reynolds stress. Here, the use of the Boussinesq eddy viscosity is assumed and formulated in terms of the turbulent kinetic energy, k , and the turbulent dissipation rate, e , or x , the specific dissipation rate. k and e/x require their own turbulent transport models [19].

The k - e and k - w turbulence models are two-equation turbulence models, which have been widely used in flow simulations. The basic principal of k - e and k - w models are to relate the eddy viscosity to k and e , or k and w , as shown below [19]: For the k - e turbulence model

$$\mu_t = \rho C_\mu \frac{k^2}{e} \quad (5)$$

where λ_t is the eddy viscosity introduced by the Boussinesq eddy viscosity assumption, C_l is an experimental constant and equal to 0.09 in this case, and ρ is the density. For the k-w turbulence model

$$\mu_t = \alpha^* \frac{\rho k}{\omega} \quad (6)$$

where ρ is the density, a is a damping coefficient, which introduces a low-Reynolds number correction, computed as follows:

$$\alpha^* = \alpha_\infty^* \left(\frac{\alpha_0^* + Re_t / R_k}{1 + Re_t / R_k} \right) \quad (7)$$

where

$$Re_t = \frac{\rho k}{\mu \omega} \quad R_k = 6 \quad \alpha_0^* = \frac{\beta_i}{3} \quad \beta_i = 0.072$$

A variety of RANS-based turbulence models are implemented in FLUENT, five of these models, the standard k-e, the RNG k-e, the realizable k-e, the SST k-w, and the Transition SST, were adopted in this study, having found use in previous flow force related investigations [11–16].

4.2 Computational Fluid Dynamics Modelling. The modelled fluid domain is identified in Fig. 5 (red dotted box). The inlet was defined at the location where the pressure sensor is mounted, and the outlet was defined at a location remote from the nozzle.

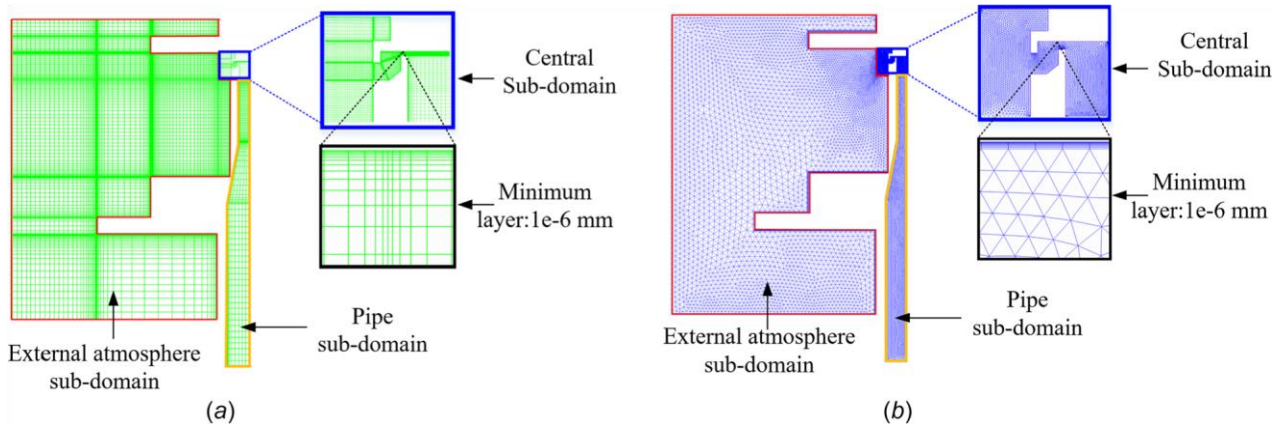


Fig. 7 Method of domain decomposition: (a) structured mesh grid and (b) unstructured mesh grid

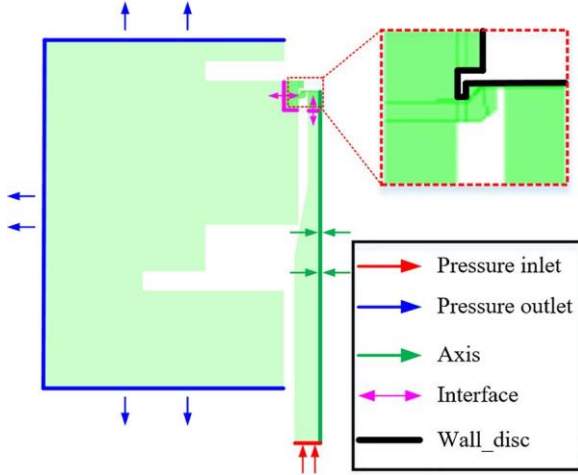


Fig. 8 Boundary conditions

Table 1 Parameters settings for simulations

Solver	Pressure-based, steady, absolute velocity formulation
Fluid	Ideal gas
Solution method	Coupled scheme Second-order
Convergence criterion	110^5 for 2D, 110^4 for 3D
Turbulence models	Standard ke RNG ke Realizable ke SST kx Transition SST

Due to the fact that the modified PSV (including the adjustment ring) has a dominant axisymmetric geometry, a 2D mesh model was developed initially. In order to identify the influence of mesh model dimensions on flow force prediction, namely, whether a 3D model is still necessary for a structure having axisymmetric features, 1/8 3D and 1/2 3D mesh models were also created, as shown in Fig. 6.

In order to control the mesh quality, the whole fluid domain was decomposed into three subdomains, namely, a pipe subdomain a central subdomain containing the seat and disk and an external atmosphere subdomain, as shown in Fig. 7. The central subdomain, containing the valve disk and the nozzle seat geometry, is the most important region for simulation. For all valve openings, this region contains many critical flow features such as rapid compressible accelerations, flow separation, choking locations, and shocks. Thus, it has the highest mesh density.

Figure 8 illustrates the boundary conditions specified in the model, including those at the inlet, the outlet, along the axis of symmetry, at fluid–structure interfaces, and at the wall–disk inter-face. Conducting CFD model validations requires that the boundary conditions of the simulations accurately reflect experimental conditions. To achieve this, the inlet was specified as a pressure outlet with a gauge static pressure value equal to 0bar, which corresponds to the atmospheric pressure.

Regarding the pressure inlet, there are two parameters that need to be specified in FLUENT, the total pressure, and static pressure. Once specified at the inlet, the total pressure will remain unchanged, while the static pressure is only used for domain initialization and will change after the iteration begins [20]. In the experiment, the static pressure at the inlet position is measured; in order to unify the conditions of the inlet, a user-defined functions

based regulating method was adopted in FLUENT to modify the inlet total pressure after every iteration, to ensure that the inlet static pressure matches the value measured by the pressure sensor.

Table 2 Density of the mesh grids for independence tests

Grid	Structured grid density (cell=mm ²)		Unstructured grid density (cell=mm ²)	
	Average	Disk region	Average	Disk region
Coarse	23.62	48.02	41.49	68.17
Fine	45.41	60.22	53.48	87.26
Very fine	75.67	115.33	90.36	128.27
Extremely fine	—	—	125.60	178.29

Fig. 9 Mesh independence test: (a) result of structured mesh and (b) result of unstructured mesh

Table 3 Mesh model Information

Model	Cells	Nodes
2D	34,376	35,504
1/8 3D	1,984,560	2,093,764
1/2 3D	5,914,261	6,110,632

For the boundary of the wall, a stationary and no-slip shear condition was set. The symmetry axis boundary is set to be an axis. The boundary conditions of the 3D mesh model are basically identical to those of the 2D model, except that the symmetry boundaries were added in the circumferential direction and the boundary of the axis was removed. In addition to the boundary conditions, the following parameters of the solver were also specified, as displayed in Table 1.

4.3 Mesh Modelling. For CFD simulations, the mesh grid density is critical to ensure the accuracy and convergence of the solver. To obtain the optimal mesh model for flow force prediction, both structured and unstructured meshes were generated and tested for the 2D model, as illustrated in Fig. 7. In order to ensure that the simulation results are independent of the mesh grid, mesh independence tests were carried out, where a total of three levels of structured grids and four levels of unstructured grids were tested.

The parameters of the tested mesh grids are shown in Table 2, in which the mesh grids were specified as coarse, fine, very fine, and extremely fine. The different levels were achieved by changing the node distribution of structured grids or changing the maximum element size of unstructured grids. The height of the first layer on walls and the growth ratio for both structured and unstructured grids are identical and equal to 110^6 mm, 1.05 and 30, respectively.

Five turbulence models were examined and adopted to predict the flow force at a 0.0011m valve opening, namely, standard $k-\epsilon$, RNG $k-\epsilon$, realizable $k-\epsilon$, SST $k-\omega$, and Transition SST. This lift was chosen for investigation because the flow pattern at this opening is the most complex. Furthermore, this valve opening is near the point where the greatest flow force gradient occurs. The results of the mesh independence tests are displayed in Fig. 9, where Eq. (1) was used to establish the indicated absolute error.

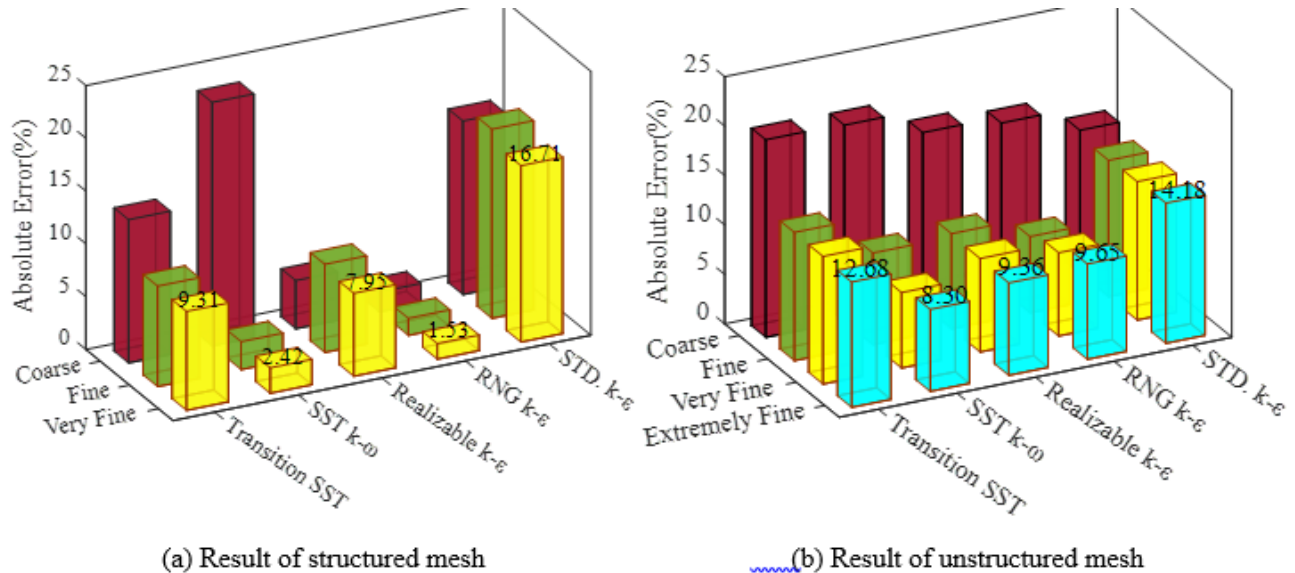


Fig. 9 Mesh independence test: (a) result of structured mesh and (b) result of unstructured mesh

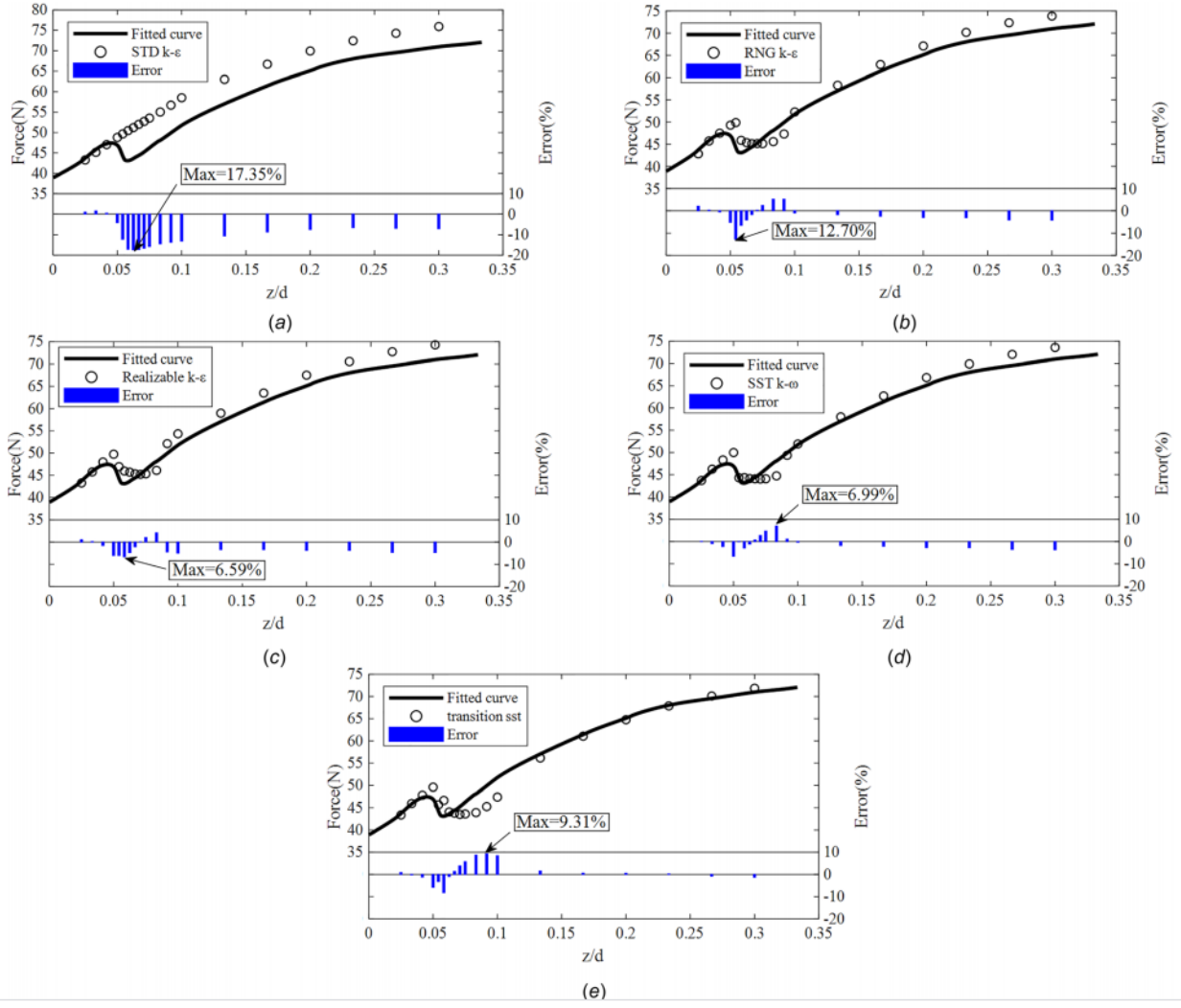


Fig. 10 Results of 2D CFD simulations: (a) standard k- ϵ model, (b) RNG k- ϵ model, (c) realizable k- ϵ model, (d) SST k-w model, and (e) transition SST model

It can be seen from Fig. 9(a) that, for all the tested turbulence models, the error varies significantly when the grid density increases from coarse to fine. As the mesh grid density continues to increase, such as from Fine to Very Fine, the error changes very little. Thus, it can be concluded that the results of the simulation are independent of the mesh grid, if the grid density is higher than the Fine level. With regard to the unstructured grid, a similar result was obtained, i.e., there are significant differences between the coarse and the fine mesh grid, while there is a slight difference among fine, very fine and extremely fine mesh levels.

It also can be seen from Fig. 9 that for a structured mesh grid of a very fine level, the error of the five turbulence models are 9.31%, 2.42%, 7.95%, 1.53%, and 16.71%, respectively, while for an unstructured mesh grid of the extremely fine level, the corresponding values are generally larger, and equal to 12.68%, 8.30%, 9.36%, 9.65%, and 14.18%, respectively. Therefore, it can be inferred that for flow force prediction, simulations with a structured mesh are, as expected, more precise than those using unstructured meshes. In summary, the Fine level structured mesh grid was deemed as the optimal choice for flow force prediction in this paper, owing to the advantages of high accuracy and a reasonable grid density.

For the 3D mesh models, all critical parameters of the 2D Fine level model, such as boundary layers, nodes distribution, and fluid domain decomposition method, remained the same. The only modification was to replicate the 2D mesh grid along the circumferential direction. A comparison of the final 2D and 3D mesh models is shown in Table 3. With the mesh models described above, a series of simulations with the different turbulence models were carried out to investigate the influence on flow force prediction.

5 Results and Discussion

The results of the 2D simulations are illustrated first to identify the optimal turbulence model. Thereafter, the results of the 3D simulations are displayed and compared to the 2D results to identify the level of geometry simplifications permitted. After that, the abilities of different CFD models for mass flow rate prediction are presented. Finally, with the results of simulations using the optimal CFD model, the phenomenon observed in the experimental result was explained.

5.1 Results: Turbulence Model Investigation. A total of five turbulence models, namely, standard k-e, RNG k-e, realizable k-e, SST k-w, and transition SST were tested. For evaluation purpose, two parameters, i.e., force value deviation and force trend, were adopted to assess the abilities of different turbulence models. The results of the force trend and value error are illustrated in Fig. 10 and Table 4, respectively.

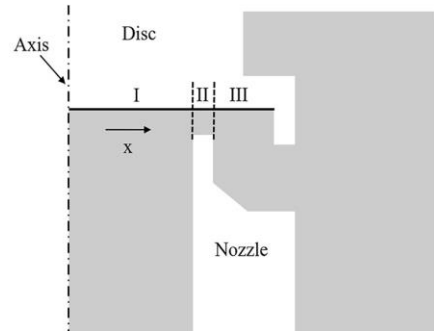
Table 4 Error for different turbulence models

Turbulence models	Maximum error (%)	Minimum error (%)	Average error (%)
Standard ke	17.35	0.46	10.06
RNG ke	12.70	0.21	3.46
Realizable ke	6.59	0.10	3.55
SST kx	6.99	0.07	2.47
Transition SST	9.31	0.21	3.29

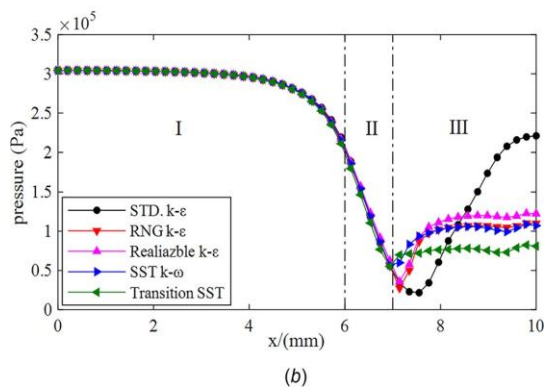
It can be seen from Fig. 10 that the experimental force trend was not monotonic and all of the turbulence models could predict it correctly, except for the standard k-e model, which produced a monotonically increasing force curve. Table 4 illustrates the results of the force deviations between the simulations and the GPR fitted curve, in which three assessment indicators, namely, maximum error, minimum error, and average error, were adopted. It can be seen that the results obtained by the various turbulence models are very different.

Examining the maximum error indicator, the maximum value is obtained by the standard k-e model and is equal to 17.35%, while the minimum value is obtained by the realizable k-e model and is equal to 6.59%. For the average error, the maximum value is also obtained by the standard k-e model, while the minimum value is obtained by the SST k-w model and is equal to 2.47%. For the maximum error, the results of the SST k-w model are close to those of the realizable k-e model, while for the average error, the SST k-w turbulence model has a lower value than the realizable k-e. Thus, the SST k-w turbulence model was deemed as the optimal for flow force predictions. It is noteworthy that the values of the minimum error indicator in Table 4 are very low, even for the standard k-e model, which means that the standard k-e model could achieve accurate results at some valve openings, for example, at an opening of $z/d < 0.05$. Therefore, it could be inferred that verifying turbulence models on flow force prediction with small samples or specific openings may result in erroneous conclusions.

To explain the force-lift results for different turbulence models, the predicted static pressure distributions on the valve disk are examined. Figure 11 illustrates the static pressure distributions on the valve disk at a $z/d = 0.10$ valve opening. To facilitate comparison, the whole fluid region was divided into three subregions, namely, I, II and III, corresponding to the region of inner nozzle, curtain and after-curtain. It is apparent that the static pressure predicted by different turbulence models in subregions I and II are very close, but differences occur in subregion III. In order to identify the cause of the difference in static pressure prediction, the flow properties obtained by different turbulence models were analyzed. Figure 12 shows the Mach number at the central subdomain region, where the black polylines represent the shapes and locations of the shockwave. It can be seen that different turbulence models produce similar flow patterns in subdomain I and II, which corresponds to the similar disk pressure distribution shown in Fig. 12. In subdomain III, where the shock/separated flow phenomena dominate, the flow properties are very different, as shown by Fig. 12. Thus, it can be inferred that the predictive ability of the different turbulence models for shock-related separation flows is the cause of the diversity of the predicted disk force.



(a)



(b)

Fig. 11 Static pressure distribution of the valve disk: (a) cross section of disk-nozzle region and (b) comparison of different turbulence model

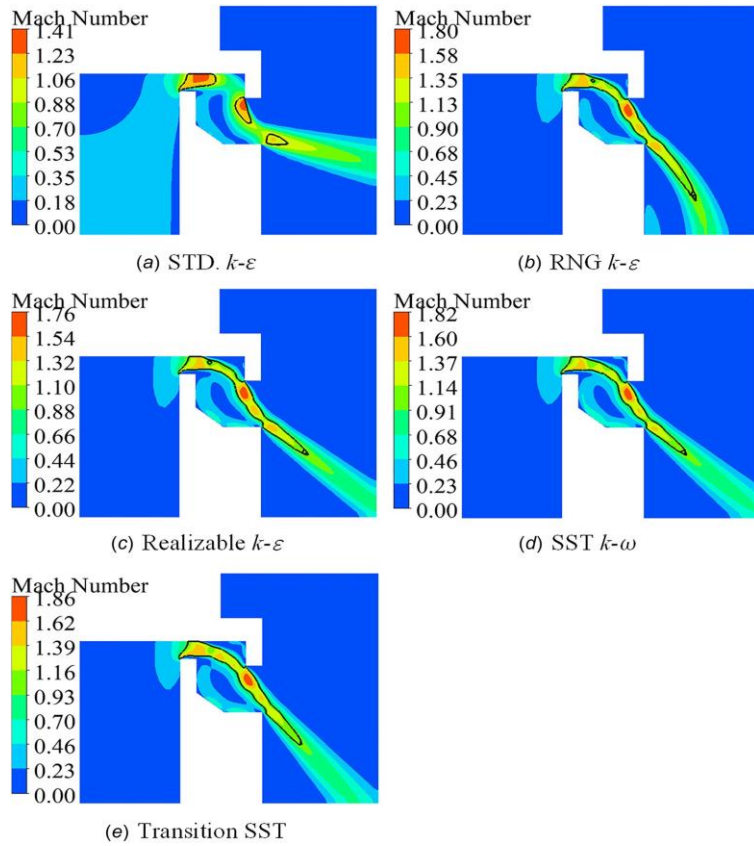


Fig. 12 Results of Mach number

5.2 Results: Geometry and Mesh Model Evaluations. For the purpose of this investigation, the effect of three different geometry models, i.e., 2D, 1/8 3D and 1/2 3D mesh models, was tested. The simulations were performed under identical solver settings, and only the optimal turbulence model, namely, SST k -w turbulence model was adopted. Figures 13(a) and 13(b) show the results of the 1/8 3D and 1/2 3D simulations, respectively. Table 5 lists the errors of each model compared to the test data.

Table 5 Results of 2D and 3D models

Mesh model	Maximum error (%)	Minimum error (%)	Average error (%)
2D	6.99	0.07	2.47
1/8 3D	4.25	0.38	2.24
1/2 3D	4.15	0.01	1.89

Regarding the force trends, both 1/8 3D and 1/2 3D simulations could predict the force trend correctly. The maximum error indices for the 1/8 3D and 1/2 3D simulations are similar with values of 4.25% and 4.15%, respectively, which are lower than for the 2D simulation. The average error indices for the 2D, 1/8 3D and 1/2 3D simulations are 2.47%, 2.24% and 1.89%, respectively. Thus, it can be inferred that for flow force prediction, simulations using 1/8 3D and 1/2 3D geometry models are more precise, and are an improvement on the 2D mesh model. In this paper, the 1/8 3D model was considered to be the optimal mesh model for flow force prediction, owing to its reasonable accuracy and mesh requirements. To explore why 3D simulations are more accurate than axisymmetric 2D simulations, the streamlines at a valve opening of $z/d = 0.08$ are compared, as shown in Fig. 14. For comparison purposes, the results of both simulations are displayed a half model by using the post processing tools of CFD post. It can be seen from Fig. 14 that the streamlines of the 2D and 1/8 3D simulations are different. For the 2D simulations, the streamline distribution along the circumferential direction is uniform and no major recirculation zone was established, while for the 1/8 3D model, recirculation is observed, and the distribution of these eddies is not uniform in the circumferential direction. At this opening, the flow force predicted by the 1/8 3D simulation is considered to be more accurate than that of the 2D simulation, and the streamlines obtained by 1/8 3D simulation are considered to be more correct in that the circumferential flow is not uniform.

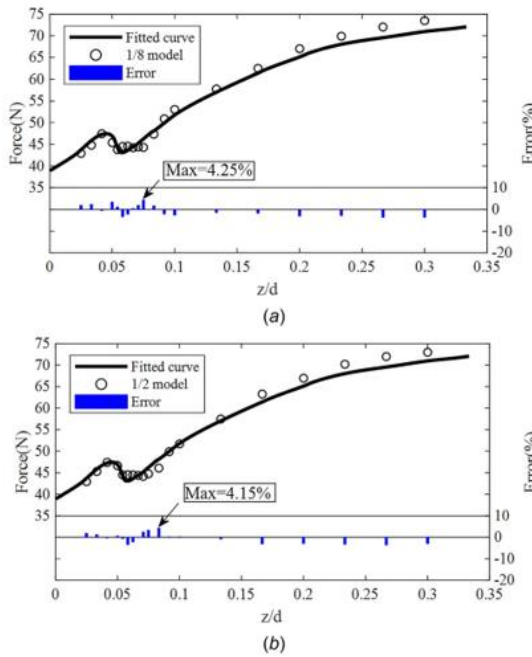


Fig. 13 Results of 3D CFD simulations: (a) 1/8 3D mesh model and (b) 1/2 3D mesh model

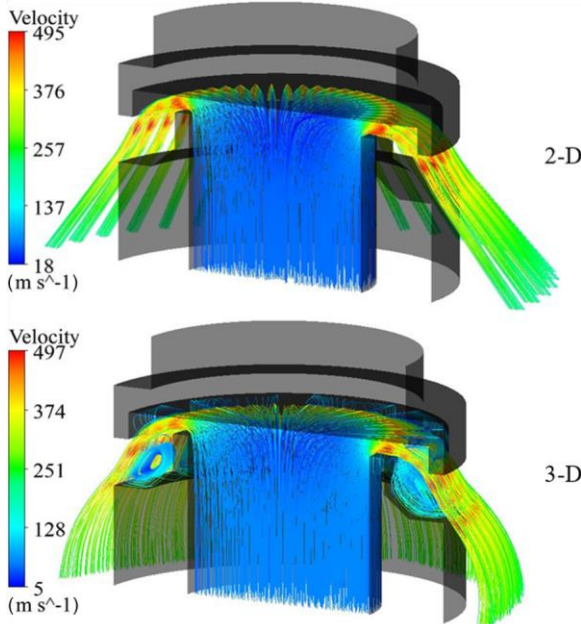


Fig. 14 Streamline of 2D and 1/8 3D simulation

In addition to the streamline, the static pressures exerted on the valve disk were also considered. In order to investigate the pressure distribution on the front face of the valve disk, the static pressure along radial lines at four angular locations is compared at a valve opening of $z/d=0.08$, as shown in Fig. 15.

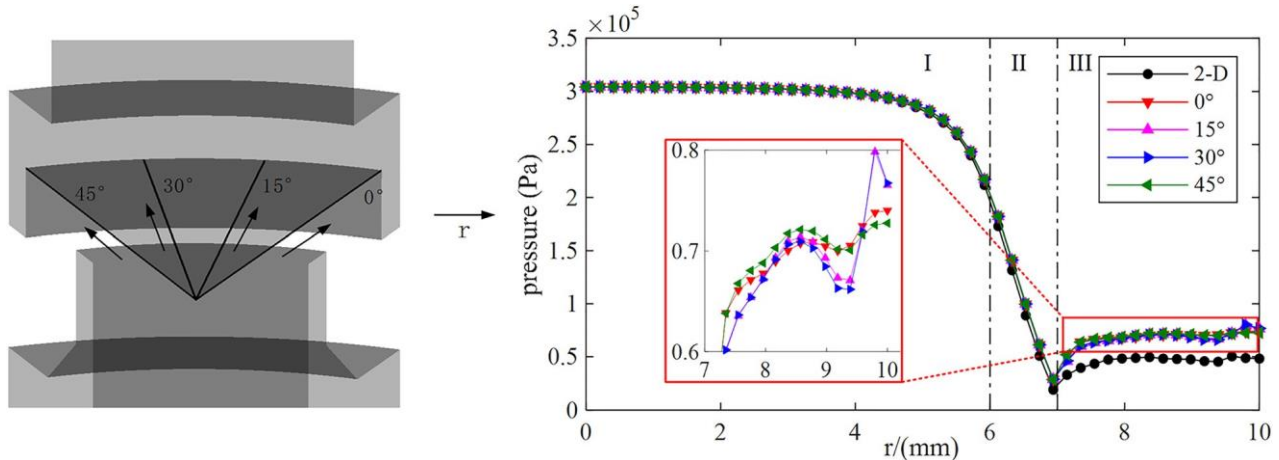


Fig. 15 Static pressure distribution

It can be seen from Fig. 15 that in regions I and II, the difference between the static pressure distributions obtained from 2D and 3D simulations is small. In region III, the static pressures predicted by the 3D model at all angle directions are higher than those of the 2D model. The flow force obtained from the 3D and 2D simulations is equal to 47.33N and 44.74N, respectively. Thus, it can be inferred that there are 3D features, such as velocity difference and pressure gradient, that exist in the circumferential direction of the flow. The 3D simulations can capture the details of these features, which are neglected by 2D simulations. This is why there is a difference between 2D and 3D simulations, for essentially an axis-symmetric geometry. These observations support the conclusion that, for flow force prediction, the 3D mesh model is necessary.

5.3 Mass Flow Rate Prediction. To examine the abilities of different CFD models to predict the mass flow rate, a series of 2D and 3D steady-state simulations were performed. Similar to the aforementioned investigations regarding the flow force, all of the five turbulence models were adopted in the 2D simulations, while only the SST k-w turbulence model was applied in 1/8 and 1/2 3D simulations.

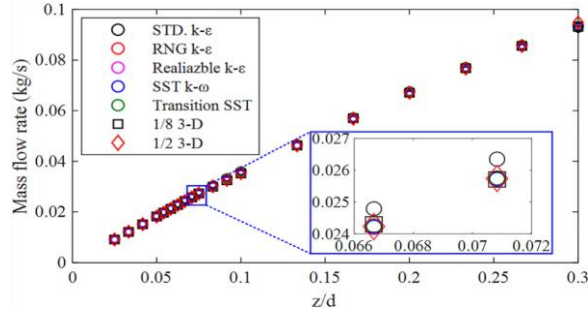


Fig. 16 Mass flow rate at different openings

Figure 16 illustrates the results of the mass flow rate obtained from the simulations. The results indicate that the mass flow rate increases monotonically with the valve opening, and the mass flow rate obtained by different turbulence models and mesh models are very similar. Thus, it can be inferred that CFD simulations with different turbulence models have similar abilities to predict the mass flow rate. In addition to the overall value of mass flow rate, the detailed nozzle flows were also considered. For compressible flow, the mass flow rate can be defined as

$$Q_m = \int_0^A \rho v dA \quad (8)$$

where Q_m is the mass flow rate, ρ denotes the density, A is the cross-sectional area, and v is the velocity. For analysis purposes, the simulation results regarding flow velocity and density at the nozzle region were extracted and compared at several valve openings. It was found that the values obtained by different CFD models are very similar. Figure 17 compares the results at a valve opening of $z/d=0.01$. It can be inferred that CFD simulations incorporating different turbulence models and geometries do not have a great influence on the predictions of the mass flow rate, although they do have an influence on flow force.

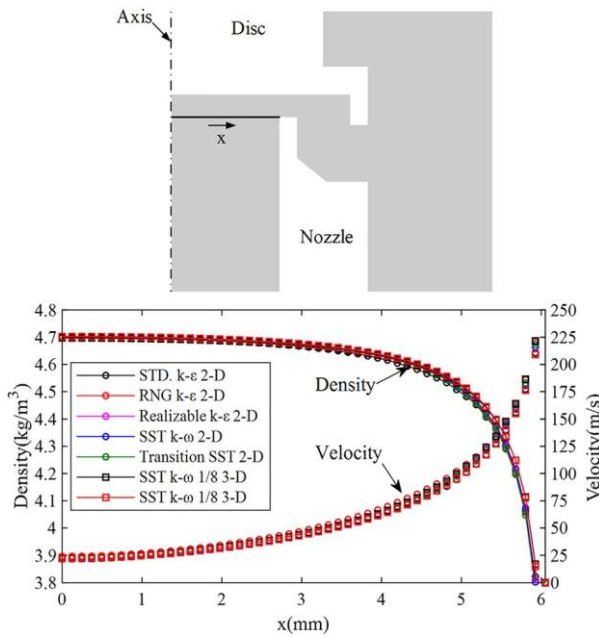


Fig. 17 Density and velocity in the nozzle region

5.4 Interpretation of the Phenomena Found in Experiments. As mentioned above, the experimental flow force is not a monotonic function of the valve opening; when $z/d < 0.04$ and $z/d > 0.05$, the flow force increases with the valve opening, while in the interval $0.04 < z/d < 0.05$, the force decreases. To clarify the causes of the force reduction, the velocity contours of six valve openings are compared in Fig. 18.

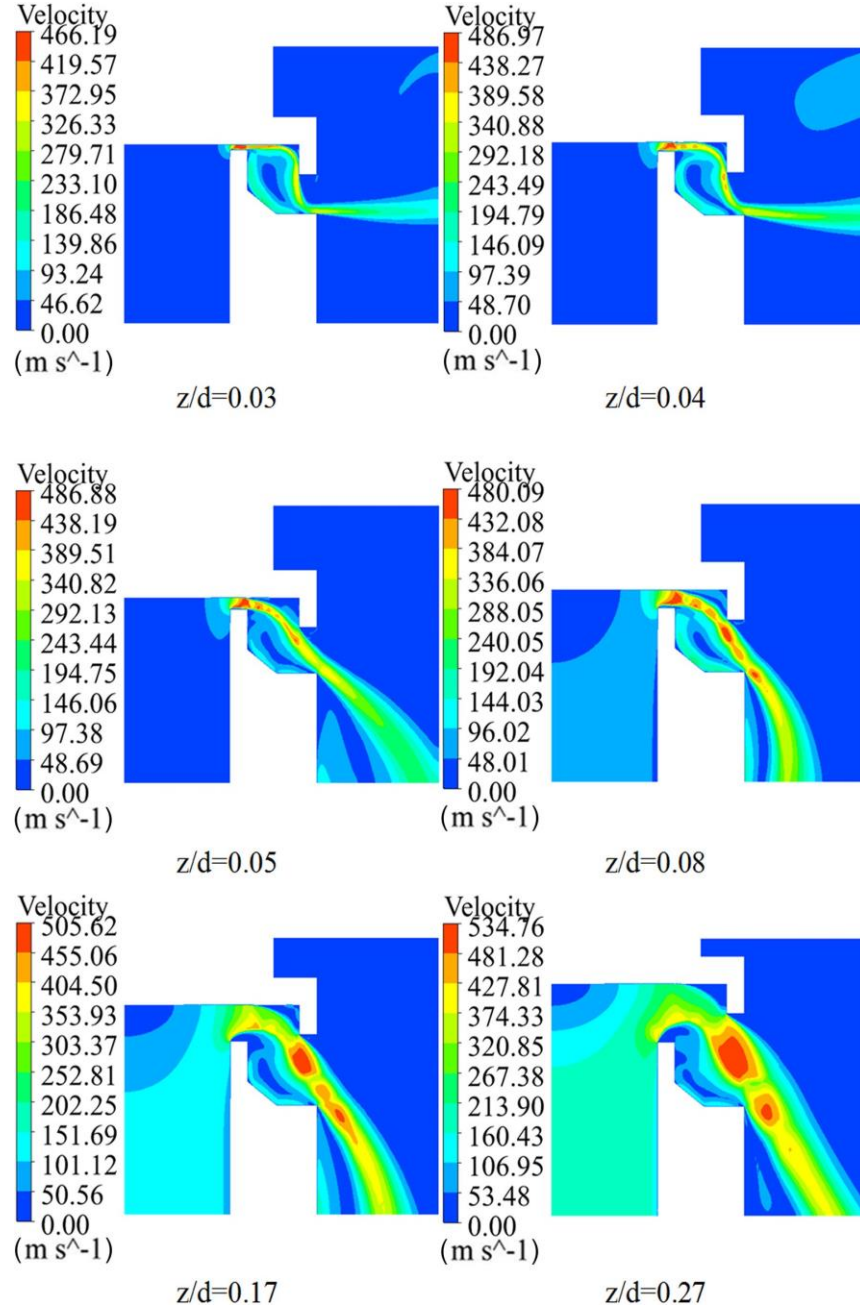


Fig. 18 Contours of velocity at different valve openings

Figure 18 illustrates that there are two dominant flow patterns, indicated by the velocity directions at the nozzle exit region. At low lifts (openings of $z/d < 0.04$), the flow at the exit is primarily horizontal, while at higher lifts (openings of $z/d > 0.05$), the flow is obliquely downward.

For additional clarification, the flow forces exerted on the valve disk at different openings are compared, as shown in Fig. 19. Here, the X-axis represents the horizontal distance from the axis of symmetry and the Y-axis, represents the flow force, established from the pressure distribution integrated on the surface of a ring, which has a thickness of 0.20mm. Figure 19(a) shows the results obtained for all of the six openings. The force trends are similar at openings for $z/d > 0.05$ or $z/d < 0.04$. Thus, it can be inferred that cases with similar flow patterns also have similar force distributions. To analyze the effect of flow pattern changes on the flow force, force

distributions for $z/d=0.04$ and $z/d = 0.05$ are compared in Fig. 19(b). It can be seen that the flow force distributions in regions I and II are similar, while in region III, the force for $z/d = 0.04$ is higher than that of $z/d = 0.05$, which suggests that the change of flow pattern is connected to the different force distributions.

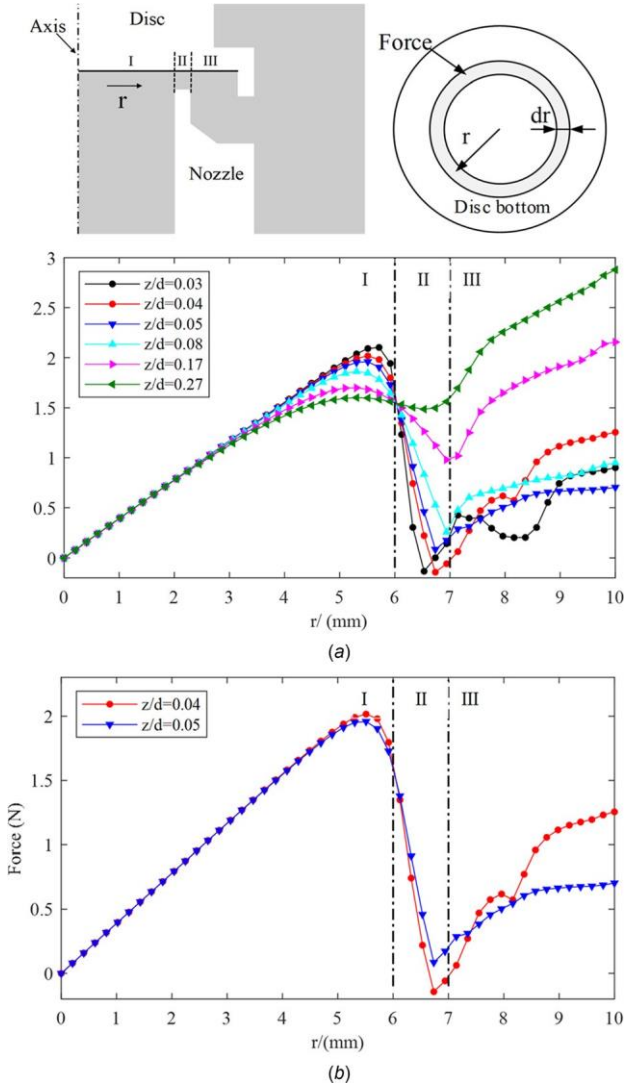


Fig. 19 Flow force at different valve openings: (a) results obtained by six openings and (b) results obtained by two openings

6 Conclusions

Many valve flow force-related investigations have been carried out by researchers using CFD methods. However, these studies focus mainly on incompressible flows, such as with hydraulic oil or water. Moreover, the adoption of various CFD models by different researchers leaves uncertainty as to which is the optimal model for the analysis of compressible flow forces. In this study, the accuracy of different CFD models for flow force prediction was investigated. For validation purposes, a test rig was developed to allow the force and mass-flow-lift characteristics to be measured. By comparing the results of these tests with CFD simulations, the accuracy of the methods and understanding of the characteristics was investigated.

The analysis and conclusions of this study can be summarized as follows:

- The performance of five turbulence model is examined by comparing the simulation results with experimental data. It was shown that the SST k-w turbulence model was the optimal choice for compressible flow force prediction.

- (ii) Both grid structure and 2D and 3D model simplifications were investigated. The results indicate that simulations with a structured grid are significantly more accurate than those with an unstructured grid model. Regarding model dimensionality, 1/8 sector 3D and 1/2 sector 3D models are shown to be more accurate than 2D models.
- (iii) It was established that with the use of 3D models and the SST k-w turbulence model, a disk force predictive accuracy better than 2% can be achieved.
- (iv) Different turbulence models and geometry models were adopted to predict the mass flow rate at identical valve openings. The results indicate that simulations with different CFD models produce similar results; i.e., the effect of the CFD model on mass flow rate prediction is not significant.
- (v) For irregular variations of force observed in the force-lift characteristics, the velocity contours and disk force distributions at different valve openings were analyzed. Flow pattern changes, which lead to variations of force distribution on the valve disk, are considered to be the causes of the flow force variations.

This study extends the current understanding of valve flow forces and the optimal CFD model requirements for accurate prediction of compressible flow force and mass flow in safety valves. However, there are still several limitations in this paper. The valve body is removed; this is at some expense to what might occur in an actual valve. Additionally, the notches of the adjustment ring are ignored, which may change the downward flow conditions, thereby affecting the flow force. These limitations will be addressed in future studies.

Funding Data

The National Natural Science Foundation of China (Grant Nos. U1608256, 51505061; Funder ID: 10.13039/501100003819).

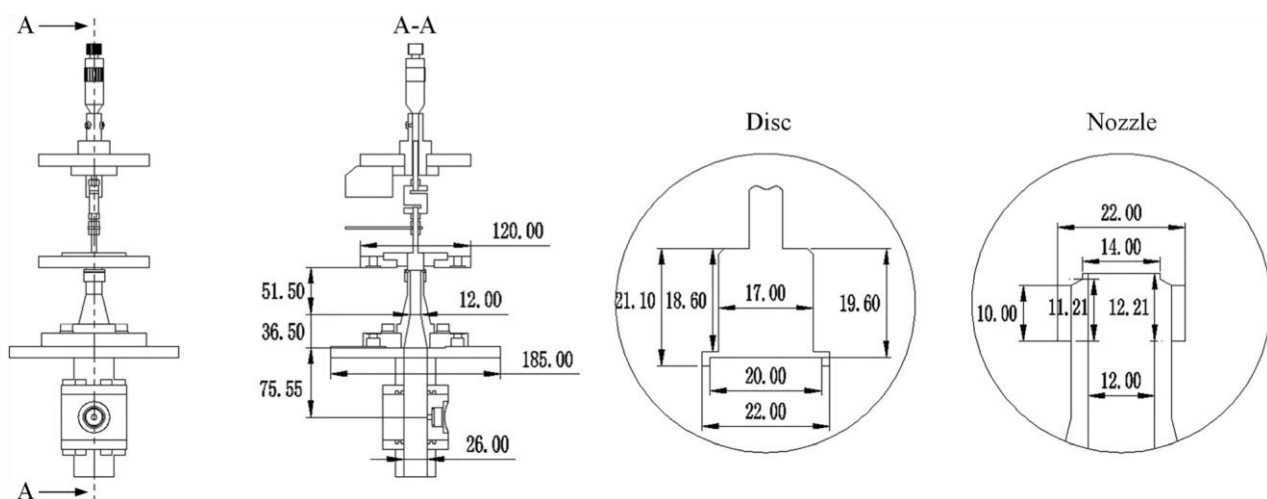
Appendix A: Experimental Data of the Lift Force Measurement

Temperature: 16+/1°C; pressure: 3bar (measured by the pressure sensor in Fig. 2(b))

Opening (mm)	Force (N)	Opening (mm)	Force (N)
0.071	39.876	0.939	47.271
0.079	40.256	0.942	46.989
0.082	40.114	0.989	48.488
0.083	39.992	0.991	47.467
0.278	43.232	1.188	51.506
0.282	43.247	1.189	51.659
0.285	43.438	1.643	57.468
0.286	43.425	1.644	57.603
0.483	47.169	1.647	57.644
0.487	47.252	1.648	57.528
0.487	47.096	2.045	61.845
0.488	47.107	2.045	61.911
0.612	46.474	2.047	61.991
0.613	46.513	2.448	65.513
0.614	46.684	2.452	65.661
0.616	46.433	2.453	65.728
0.667	43.229	2.455	65.657
0.668	43.348	2.842	68.235
0.671	43.115	3.254	69.738
0.683	43.220	3.651	71.240
0.770	43.991	3.651	71.021
0.838	44.848	3.845	71.603
0.839	45.192	3.846	71.583
0.937	46.921		

Appendix B: Specific Geometrical Parameters (in Millimeters) of the Modified Pressure Safety Valve

The dimensions are measured with a micrometer after processing; thus, only the two digits after the decimal point are retained.



References

- [1] Darby, R., 2013, "The Dynamic Response of Pressure Relief Valves in Vapor or Gas Service—Part I: Mathematical Model," *J. Loss Prev. Process Ind.*, 26(6), pp. 1262–1268.
- [2] Song, X. G., Cui, L., Cao, M. S., Cao, W. P., Park, Y. C., and Dempster, W. M., 2014, "A CFD Analysis of the Dynamics of a Direct-Operated Safety Relief Valve Mounted on a Pressure Vessel," *Energy Convers. Manage.*, 81, pp. 407–419.
- [3] Fromann, O., and Friedel, L., 1998, "Analysis of Safety Relief Valve Chatter Induced by Pressure Wave in Gas Flow," *J. Loss Prev. Process Ind.*, 11, pp. 279–290.
- [4] Aldeeb, A. A., Darby, R., and Arndt, S., 2014, "The Dynamic Response of Pressure Relief Valves in Vapor or Gas Service. Part II: Experimental Investigation," *J. Loss Prev. Process Ind.*, 31, pp. 127–132.
- [5] Song, X. G., Wang, L. T., Park, Y. C., and Sun, W., 2015, "A Fluid-Structure Interaction Analysis of the Spring-Loaded Pressure Safety Valve During Popping Off," *Procedia Eng.*, 130, pp. 87–94.
- [6] Song, X. G., Wang, L., and Park, Y. C., 2010, "Transient Analysis of a Spring-Loaded Pressure Safety Valve Using Computational Fluid Dynamics (CFD)," *ASME J. Pressure Vessel Technol.*, 132(5), p. 054501.
- [7] Hos, C. J., Champneys, A. R., Paul, K., and McNeely, M., 2014, "Dynamic Behavior of Direct Spring Loaded Pressure Relief Valves in Gas Service: Model Development, Measurements and Instability Mechanisms," *J. Loss Prev. Process Ind.*, 31, pp. 70–81.
- [8] Darby, R., and Aldeeb, A. A., 2014, "The Dynamic Response of Pressure Relief Valves in Vapor or Gas Service—Part III: Model Validation," *J. Loss Prev. Process Ind.*, 31, pp. 133–141.
- [9] Duan, Y., Eaton, M. D., Bluck, M. J., and Jackson, C., 2018, "A Validation of CFD Methods on Predicting Valve Performance Parameters," *ASME Paper No. POWER 2018-7434*.
- [10] Duan, Y., Jackson, C., Eaton, M. D., and Bluck, M. J., 2019, "An Assessment of Eddy Viscosity Models on Predicting Performance Parameters of Valves," *Nucl. Eng. Des.*, 342, pp. 60–77.
- [11] Lisowski, E., Czyzycki, W., and Rajda, J., 2013, "Three Dimensional CFD Analysis and Experimental Test of Flow Force Acting on the Spool of Solenoid Operated Directional Control Valve," *Energy Convers. Manage.*, 70, pp. 220–229.
- [12] Simic, M., and Herakovic, N., 2015, "Reduction of the Flow Forces in a Small Hydraulic Seat Valve as Alternative Approach to Improve the Valve Characteristics," *Energy Convers. Manage.*, 89, pp. 708–718.
- [13] Amirante, R., Moscatelli, P. G., and Catalano, L. A., 2007, "Evaluation of the Flow Forces on a Direct (Single State) Proportional Valve by Means of a Computational Fluid Dynamic Analysis," *Energy Convers. Manage.*, 48(3), pp. 942–953.
- [14] Scuro, N. L., Angelo, E., Angelo, G., and Andrade, D. A., 2018, "A CFD Analysis of the Flow Dynamics of a Directly-Operated Safety Relief Valve," *Nucl. Eng. Des.*, 328, pp. 321–332.
- [15] Asim, T., Charlton, M., and Mishra, R., 2017, "CFD Based Investigations for the Design of Severe Service Control Valves Used in Energy Systems," *Energy Convers. Manage.*, 153, pp. 288–303.
- [16] Dempster, W. M., Lee, C. K., and Deans, J., 2006, "Prediction of the Flow and Force Characteristics of Safety Relief Valves," *ASME Paper No. PVP2006ICPVY-11-93142*.
- [17] Dempster, W. M., and Alshaikh, M., 2018, "CFD Prediction of Safety Valve Disc Forces Under Two Phase Flow Conditions," *ASME Paper No. PVP2018-84745*.
- [18] API, 2014, "Sizing, Selection, and Installation of Pressure-Relieving Devices—Part I: Sizing and Selection," American Petroleum Institute, Washington, DC, Standard No. STD 520 P1.
- [19] ANSYS Inc., 2019, "ANSYS Documentation, Fluent, Turbulence, 4.0," ANSYS, Canonsburg, PA.
- [20] ANSYS Inc., 2019, "ANSYS Documentation, Fluent, Defining Total Pressure and Temperature, 6.3.3.1.1.2," ANSYS, Canonsburg, PA.